

Graded Coronagraphic Masks for High-Contrast Near-Infrared Imaging

Joseph C. Carson^{a,b}, Daniel W. Wilson^b, John T. Trauger^b

^aCalifornia Institute of Technology, Pasadena, CA, USA 91125;

^bJet Propulsion Laboratory, Earth & Space Sciences, 4800 Oak Grove Dr., Pasadena, CA, USA 91109;

ABSTRACT

We present here results from an experimental and theoretical study in the use of graded focal-plane occulting masks to improve high-contrast astronomical imaging at near-infrared wavelengths. The study includes investigations of both high-energy beam sensitive (HEBS) glass (a product of Canyon Materials, San Diego, CA) and binary notch-filter technologies to create precision graded occulting masks. In conjunction with this investigation, we conduct computer simulations showing expected high-contrast levels for various graded masks being considered for installation in the PHARO camera of the Palomar 200-inch (5m) Hale Telescope Adaptive Optics (AO) system. Our results demonstrate that the implementation of a graded exponential mask in the Palomar system should improve high-contrast sensitivities by about 2.3-mag in K-band (2.0-2.4 μm), for 0.75-1.5 arcsec separations. We also demonstrate that both HEBS and binary notch-filter technologies present adequate platforms for necessary occulting requirements. We conclude with a discussion of the insights our study yields for planned space-based high-contrast observatories such as NASA's planned Terrestrial Planet Finder Coronagraph (TPF-C) and the proposed Eclipse mission.

Keywords: occulting spots, coronagraphs, high-contrast imaging, graded coronagraphic masks

1. INTRODUCTION

In the last decade, a desire to successfully take the first exo-solar planet images has fueled a strong community effort in extreme high-contrast imaging: in the area of ground-based imaging, Oppenheimer et al. (2004) describe implementation of a high-contrast imaging system for use with the US Air Force Advanced Electro-Optical System; in the space-based arena, NASA's planned Space Interferometry Mission uses nulling interferometry to image larger planets around nearby stars (Shao, 2004); NASA's planned Terrestrial Planet Finder (TPF) missions, with a visible/near-infrared coronagraphic component (TPF-C) along with a mid-infrared interferometric component (TPF-I), offer the capability of detecting earth-sized masses around stars ("Technology Plan for the Terrestrial Planet Finder", 2003). In support of TPF-C research and development, Jet Propulsion Laboratory (JPL) developed the High Contrast Imaging Testbed (HCIT; Trauger et al. 2004), a vacuum environment, active optics testbed where numerous focal plane graded masks are tested in a simulated extreme high-contrast optical-wavelength imaging environment. JPL's HCIT team, of which this paper's authors are members, currently tests a range of graded mask patterns, including Gaussian functions, sinc² functions and various band-limited masks (see Kuchner & Traub, 2002 and Kuchner, Crepp, & Ge, 2004). Positive results from these experiments (Trauger et al., this conference) fueled the investigation into graded masks for ground-based, high-contrast, near-IR applications, which we describe in this paper.

Two promising technologies have emerged as potential candidates for near-IR precision graded masks: binary notch-filter masks and HEBS glass. Binary notch-filter masks are a relatively mature technology where a clear substrate such as fused silica is coated with an opaque surface layer such as an Aluminum film. Through electron-beam lithography exposure, stripes of aluminum can be "lifted off" to effectively create a graded transmission function. Debes et al. (2004) demonstrate how such masks can effectively be used for high-contrast imaging at optical wavelengths. In this paper we examine its appeal for graded coronagraphic imaging at near-IR wavelengths.

Lead Author Contact: Joseph.Carson@jpl.nasa.gov; 818-354-0674

Techniques and Instrumentation for Detection of Exoplanets II, edited by Daniel R. Coulter, Proceedings of SPIE Vol. 5905 (SPIE, Bellingham, WA, 2005) · 0277-786X/05/\$15 · doi: 10.1117/12.615935

In the last five years, HEBS glass has surfaced as a possible alternative to binary technologies. It entails the use of a clear low expansion zinc-borosilicate glass with a silver-ion-doped surface layer. Exposure to high energy (greater than ~ 10 keV) electron beams causes specs of silver atoms to darken the glass (www.canyonmaterials.com). Since electron beams routinely focus down to $0.1 \mu\text{m}$ (Wilson et al. 2003), they offer more precise pattern writings than typical binary masks ($\sim 0.25 \mu\text{m}$ precision [Debes et al. 2004]). Furthermore, they offer a true grayscale photomask as opposed to a halftone binary mask. But while exhibiting excellent performance at optical wavelengths (see Wilson et al. 2003), HEBS glass use at near-IR wavelengths is largely an un-tested technology. In this paper we present some of the first results of HEBS glass performance at near-IR wavelengths.

The Palomar 200 inch (5 m) Hale Telescope offers an ideal environment to take advantage of these advances in graded focal plane mask technologies. Its high order adaptive optics system (PALAO; Troy et al. 2000) and accompanying PHARO science camera (Hayward et al. 2001) offer diffraction limited imaging with selectable focal plane and pupil plane masks; currently, the user may select between a 0.41-arcsec and a 0.91-arcsec coronagraphic spot with one of three conventional pupil plane Lyot masks, a Large, Medium, and Standard Cross. To date, the system has proved an effective tool to conduct high-contrast observational searches such as explorations for faint substellar companions to nearby stars (Carson et al. 2005; Metchev & Hillenbrand 2004). However, the lack of any graded occulting mask provides a ripe opportunity for high-contrast improvements through a study such as this one. Taking advantage of this fact, we present results from detailed simulations of the Palomar AO system with a variety of hypothetical focal plane masks installed. We summarize the results of these simulations in Section 2. Section 3 presents our laboratory studies of HEBS and binary masks. Section 4 presents our conclusions and final thoughts.

2. PALOMAR ADAPTIVE OPTICS CORONAGRAPHIC SIMULATIONS

2.1. Simulation Code - General Overview

Our Palomar simulations utilize a Fraunhofer diffraction model where we use a tapered, high pass filter in spatial frequency space (following Sivaramakrishnan et al. 2001) to simulate the effects of adaptive optics wavefront correction. The code represents an adaptation of code written by Chris Koresko (JPL) to model four-quadrant phase masking on the Palomar AO system (see Haguenaer et al., this conference). The simulation begins with a uniform wavefront convolved with a Kolmogorov phase mask, representing atmospheric distortion. For our simulated atmosphere, we used a Fried parameter of 20 cm. Subsequent tests showed this value to be adequate for accurately modeling current Palomar AO data. After convolving the resultant wavefront with a modeled telescope pupil and secondary mirror obscuration (including mirror supports), we implement a parabolic filter (from Sivaramakrishnan et al. 2001) to mimic the effects of the AO system. We run the simulation multiple times at different sampled wavelengths. The wavelength dictates the effective scale of the Kolmogorov spectrum as well as the dimensions of the telescope pupil and secondary obscurations (as described in units of wavelength per pupil diameter). We average the resultant individual point spread functions (PSF) to create the composite polychromatic PSF. Finally we apply two sinusoidal ripple patterns, each propagating in orthogonal directions across the pupil plane, in order to simulate a peculiar property of the Palomar AO deformable mirror algorithm, which results in a characteristic “waffle pattern” in the final image plane PSF (see Figure 1). We convolve the resultant function with various transmission masks representing potential graded focal plane masks. Fourier-transforming to the pupil plane, we next apply a Lyot mask, representing one of three Lyot masks currently available in the PHARO camera. Fourier transforming back to the image plane, we measure the resultant intensity, thus arriving at the expected detector science image. In this study we present PSFs from K-band image models, but results should largely be applicable to J and H bands. Figure 1 displays sample modeled PSFs compared with real images collected at the telescope.

The simulation judges the efficacy of a given sampled mask by first converting the outputted PSF into a corresponding “sensitivity” map. The “sensitivity” map approximates, for a given modeled coronagraph, the faintest detectable source that can be gleaned from around our bright source. The algorithm accomplishes this by sampling each pixel in the PSF image and measuring the standard deviation in a $3\text{-pixel} \times 3\text{-pixel}$ box centered on that pixel. This standard deviation is recorded as an effective “noise” value. It is not a fundamental noise since, for instance, a well-ordered PSF slope will be misread as random noise. However, this method serves as a useful

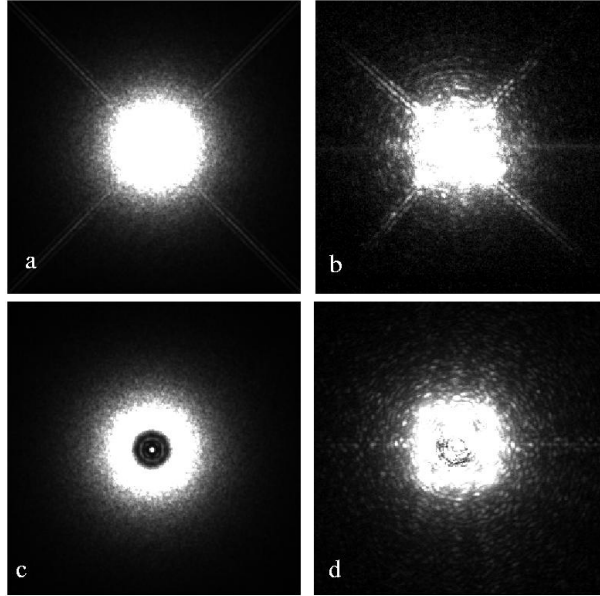


Figure 1. A comparison of Palomar K-band AO PSFs generated by simulations (frames on the left side) and images collected on-telescope (frames on the right). Each field of view represents $\sim 7.4\text{-arcsec} \times 7.4\text{-arcsec}$. Frame *a*: simulation-generated image representing the PHARO Standard Cross and no occulting mask. Frame *b*: on-telescope image taken with the Standard Cross and no occulting mask. Frame *c*: simulation-generated image representing a 0.91-arcsec spot and the PHARO standard cross. Frame *d*: on-telescope image taken with a 0.91-arcsec spot and Standard Cross.

approximation, given the requirements of this study. The faintest detectable hypothetical target signal should be roughly proportional to this “noise” value. And since we only care about the relative sensitivity between different simulated coronagraphs, the absolute signal remains irrelevant as long as we have this proportional value. Therefore, by mapping out the “noise” as a function of radial separation, for two competing scenarios, we can meaningfully compare the relative sensitivities to faint nearby objects. When doing this, we make sure to account for any removal of companion target flux by either the focal-plane or pupil-plane masks.

2.2. Simulated PSFs versus Real Telescope PSFs

Figures 2 and 3 represent radial intensity profiles of the Figure 1 data. One sees, in those radial plots, that the telescope and simulation data match up best for separations greater than $\sim 0.75\text{-arcsec}$. Considering the poorer model predictions for $<0.75\text{-arcsec}$ separations, we decided to only examine high-contrast sensitivities for $\geq 0.75\text{-arcsec}$ separations.

2.3. Graded Mask Functions

For our focal plane mask simulations, we examined four types of graded masks: exponential, Gaussian, sinc^2 , and 8th-order masks. Publications such as Kuchner & Traub (2002) and Kuchner, Crepp, & Ge (2004) have demonstrated the superiority of sinc^2 and 8th-order masks for off-axis telescope systems. Since the Palomar system, in contrast, possesses a secondary mirror obscuration, secondary mirror supports, and set Lyot stop sizes, it is not a given that the sinc^2 and 8th-order masks will be effective for our applications. Accordingly, we rely on the results of our simulations to determine their efficacy.

The exponential mask consists of an opaque coronagraphic spot with an exponential drop-off at the edges. For separations less than r_{spot} , transmission equals zero. Outside of r_{spot} , the amplitude transmission equals the following:

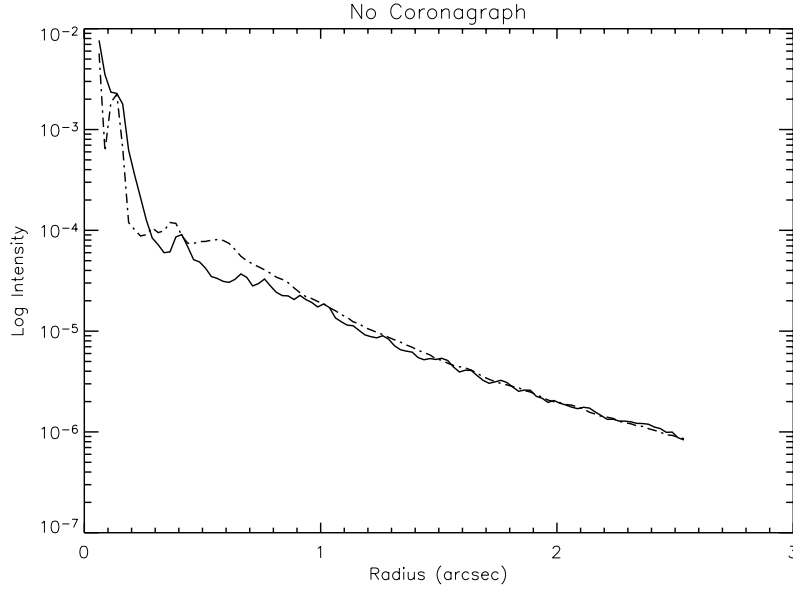


Figure 2. Radial intensity plots of data shown in figures 1a and 1b (Standard Cross, no focal plane occulting mask). The dashed curve represents simulated data while the solid curve represents on-telescope data. We normalize each intensity function so that the total intensity under the curve equals unity. For less than ~ 0.3 -arcsec, the simulated PSF displays a slightly narrower core with greater structure. This may result from the fact that the on-telescope curve represents a median combination of several PSFs where internal instrument flexure (resulting in position differences between consecutive frames) may have caused the core features to effectively broaden. The discrepancy between model and experimental data at ~ 0.6 -arcsec coincides with the outer radius at which the AO system is able to correct the natural-seeing PSF. Sivaramakrishnan et. (2001) describe a similar phenomenon in their simulations. Outside of ~ 0.75 -arcsec, however, the model and experimental data match-up well enough to allow the simulated data to provide a useful probe of predicted AO-corrected PSFs.

$$T(r) = 1 - e^{(r-r_{spot})/sg} \quad (1)$$

$T(r)$ represents amplitude transmission as a function of radius, r , from the spot center, in units of arcseconds. sg is a characteristic constant. For our tests we examine r_{spot} values of 0 to 0.6-arcsec at 0.1-arcsec intervals. For each sampled spot radius, we test sg values ranging 100 to 400 at intervals of 50.

Our Gaussian masks follow the form:

$$T(r) = 1 - e^{-\frac{1}{2}(r/sg)^2} \quad (2)$$

As in Equation 1, $T(r)$ is the amplitude transmission as a function of radius, r , in units of arcsec, from the mask center; sg , again, is a characteristics constant. Our tests examine sg values ranging from 10 to 100 at intervals of 10.

Our sinc^2 masks follow the form:

$$T(r) = 1 - \text{sinc}^2\left(\frac{a}{r}\right) \quad (3)$$

$T(r)$ and r follow the previous conventions; a is a characteristic constant. Our simulations test a values of 3, 4, 5, 10, 20, 30, 40, 50, 100, 150, 200, and 1000.

Our 8th-order masks, following Kuchner et al. (2004), are described by one of two functions:

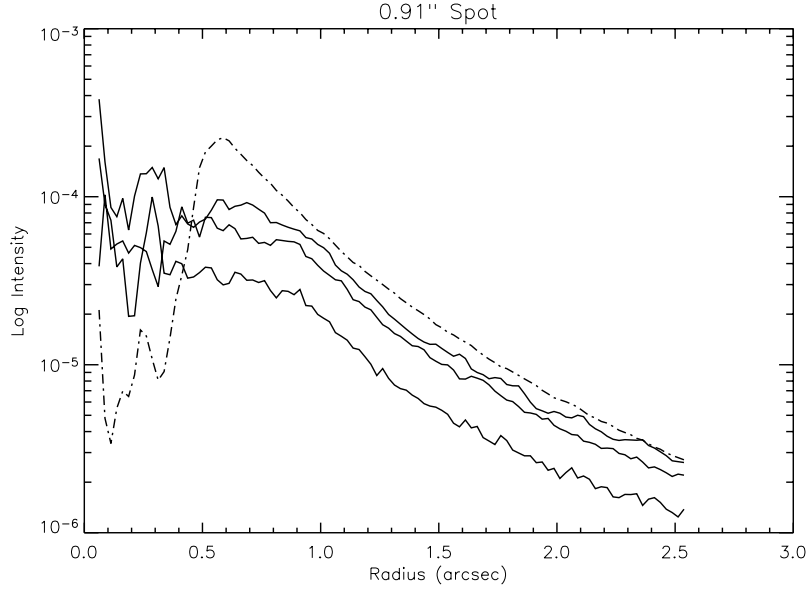


Figure 3. Radial intensity plots of data shown in figures 1c and 1d (standard cross, 0.91-arcsecond coronagraphic spot). The dashed curve represents simulated data. The solid curves represent three sample on-telescope PSFs. Each intensity function was normalized so that the total area under each curve equals unity. One notices that the simulated data predicts slightly larger-intensity PSF wings than the experimental data, though overall shape is similar. This results mainly from the fact that our simulated inner core (less than ~ 0.4 -arcsec) predicts a smaller total flux level than the experimental data. This effectively results in the PSF wings being over-emphasized (compared to the experimental data) during the normalization process. For our simulations however, where we compare different radial intensity plots generated from a single modeled source brightness transmitted through sampled focal plane masks, no normalization is required. Hence, the observed discrepancy in the up-down offset of the wings would likely have a minimal effect on our ability to simulate relative focal plane mask performance.

$$T(r) = N\left(\frac{l-1}{l} - \text{sinc}^l\left(\frac{\pi r \epsilon}{l \lambda_{max} f}\right) + \frac{1}{l} \text{sinc}\left(\frac{\pi r \epsilon}{\lambda_{max} f}\right)\right) \quad (4)$$

or

$$T(r) = N\left(\frac{3n-1}{3n} - \text{sinc}^n\left(\frac{\pi r \epsilon}{n \lambda_{max} f}\right) + \frac{1}{3n} \text{cosc}\left(\frac{\pi r \epsilon}{n \lambda_{max} f}\right)\right) \quad (5)$$

In these equations λ_{max} is the maximum encountered wavelength. Since we are considering K-band (2.00-2.40 μm) wavelengths in this particular simulation, we set $\lambda_{max} = 2.40\text{-}\mu\text{m}$. n and l represent characteristic constants. Following the protocol in Kuchner et al. (2004), our simulations sample $n = 1, 2, 3, 4, 5$ and $l = 2, 3, 4$. ϵ represents a bandwidth, defined in Kuchner et al. as the fraction of the telescope pupil masked off by the pupil-plane Lyot mask. This definition highlights an obstacle in trying to apply 8th-order masks to the Palomar Hale Telescope. Kuchner et al. conduct their calculations for an off-axis telescope (modeled along the lines of NASA's planned TPF-C space telescope, with no secondary mirror obscurations). The Palomar Hale Telescope, in contrast, possesses Lyot masks which mask off both the telescope pupil's outer edge as well as obscurations introduced by the secondary mirror and its corresponding support structures. Fabrication of new novel pupil-plane Lyot masks is beyond the considerations of this paper. Given current limitations, we settle on sampling ϵ values of 0.045, 0.168, and 0.360, representing the PHARO camera's Large, Medium, and Standard Cross, when one ignores the fraction masked off for the secondary mirror obscurations.

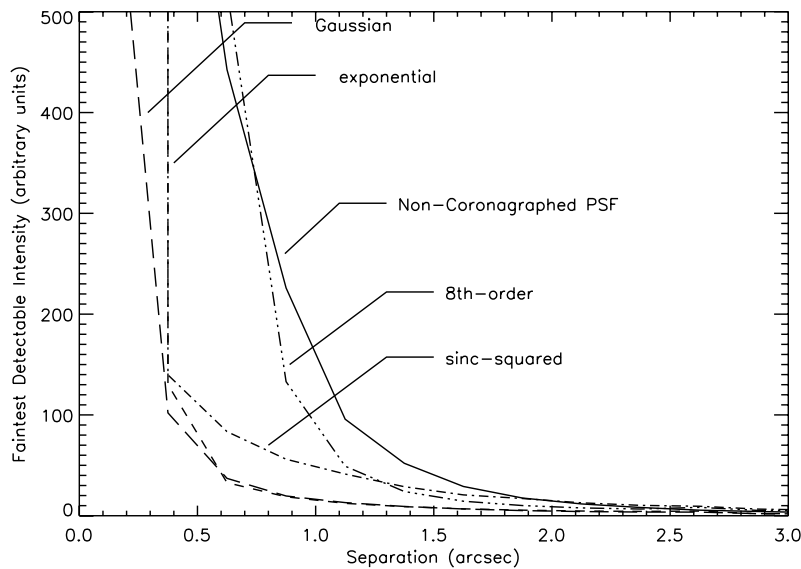


Figure 4. Sensitivity plots for a non-coronagraphed PSF (solid curve) and a PSF covered by one of four mask types: exponential (long-dashed curve; spot diam=0.6-arcsec, $sg=400$), Gaussian (short-dashed curve; $sg=100$), sinc^2 (dot-dashed curve; $a=100$), 8th-Order (dot-dot-dot-dashed curve; $l=2$). The curves represent the minimum-intensity source that could be identified near a coronagraphed PSF at a separation represented by x-axis values. Since we only wish to compare adjacent curves, rather than predict true detectable magnitudes, we sufficed to represent the y-axis in arbitrary units. The precise values on the y-axis would depend on the specific parent star brightness, seeing conditions, etcetera. All aforementioned mask parameters represent the optimal values that produce the best high-contrast sensitivities, as determined from our simulations. One sees that the exponential and Gaussian masks deliver the best sensitivities, with the sinc^2 and 8th-order masks lagging significantly behind. All curves represent the PHARO Standard Cross Lyot stop, which, in all simulated cases, performed equal or better to the other available Lyot stops.

2.4. Simulation Results

Using the masks and parameters described in Section 2.3, we wrote our simulations to select, for every given graded mask type (exponential, Gaussian, sinc^2 , or 8th-order), the set of parameters that resulted in the best sensitivities at separations between 0.75 and 1.5 arcsec. Trial and error taught us that this region offered the greatest potential for high-contrast improvement, compared to PHARO's current 0.41-arcsec and 0.91-arcsec masks. We allowed the code to sample through all available PHARO Lyot stops (Standard, Medium, and Large) when finding the best mask parameter combination). Figure 4 displays our highest achievable sensitivity curves for each graded mask type, over-plotted with model data for a non-coronagraphed PSF (and Standard Cross). The exact best mask transmission curves, with their listed parameters, can be seen in Figure 5. The Gaussian mask, with $sg=100$, and the exponential mask (spot diam=0.6-arcsec; $sg=400$) exhibit the best sensitivities. The sinc^2 ($a=200$) mask and 8th order mask ($l=2$) lag noticeably behind those. All graded masks exhibit significant improvement compared to the 0.91-arcsec spot, PHARO's current best-performing coronagraphic mask (as determined by J. Carson from on-telescope tests in summer 2004). Over 0.75-1.5 arcsec separations, for instance, the Gaussian, exponential, sinc^2 , and 8th-order masks, respectively, demonstrate sensitivity improvements of 2.3-mag, 2.2-mag, 1.0-mag, and 0.5-mag, compared to the 0.91-arcsec coronagraphic spot. An examination of the Figure 5 curves shows that the simulation, which searches for the mask parameters that produce the best sensitivities, selects parameters that cause all masks to converge to what looks like a single Gaussian or exponential shape. Hence, the introduction of the more complex sinc^2 and 8th-order mask do not seem to have a noticeable improving effect compared to the simpler Gaussian or exponential gradient.

As a final test, we examined how limits in the occulting mask maximum optical depth affects sensitivity

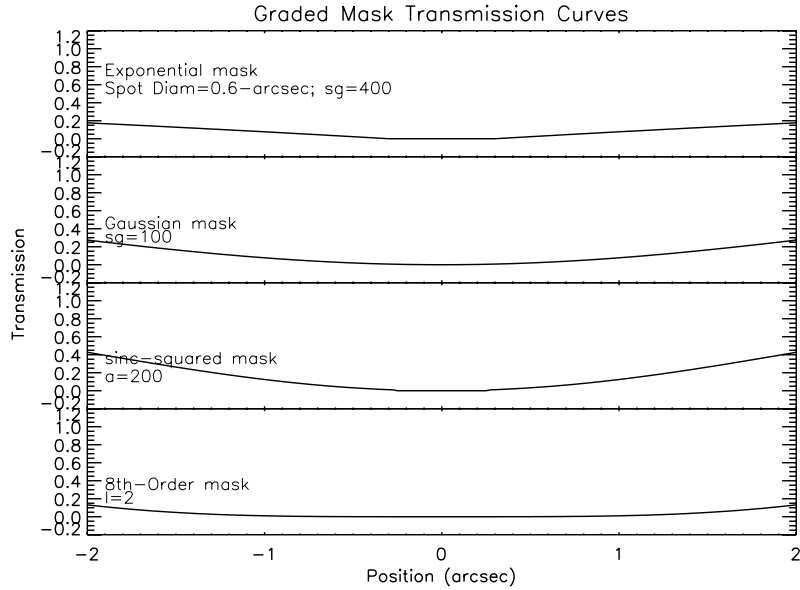


Figure 5. Transmission plots for the four optimum graded mask types.

levels. Up to now, we have assumed that our occulting masks can possess infinite opacity. But experience tells us that particular mask substrates, HEBS glass most noticeably, have limiting opacity levels. To address this issue, we simulated our best-case Gaussian occulter, but using maximum optical depths of 2, 4, 6, and 8. Only the optical depth (OD) of 2 exhibited any noticeable change in achievable sensitivity. And even then, the change could only be seen for ≤ 0.5 -arcsec separations.

Finally, we examined how changes in opacity resolution affect achievable sensitivities. As we shall discuss in Section 3, binary notch-filter masks typically allow for the fabricator to create features with $0.25\text{-}\mu\text{m}$ resolution. At the PHARO occulting mask plane, that corresponds to 0.6-mas . Our models simulate an occulting mask using 25-mas pixel resolutions, a resolution equivalent to the science array pixel scale. Since a binary mask grey scale must be built up from a series of light and dark spots, the opacity resolution of a 25-mas element should be no better than $\sim 2.5\%$. We therefore modified our best-case Gaussian mask so that all transmission values were rounded off to the nearest integer-multiple of 2.5% . Our results indicated no noticeable change in achievable sensitivities.

3. BINARY NOTCH-FILTER AND HEBS GLASS EXPERIMENTS

This laboratory study examines two competing graded mask technologies, HEBS glass and binary notch-filter masks. As described in Section 1, binary mask fabrication, a more mature technology, begins with a clear glass substrate (CVI PW-1012UV fused silica for our tests) with an opaque surface coating (Al for our tests). Stripes of Al are then “lifted off” using electron gun photolithography. By appropriately manipulating the width and spacing of stripes, an effective gray-scale can be built. HEBS glass fabrication, as described in Section 1, involves electron beam gun exposure of a zinc-borosilicate glass with a silver-ion-doped surface layer. Upon exposure, the silver ions induce an opaqueness allowing for a true grey-scale and more precise writing patterns (again see Section 1). While tested and documented (Wilson et al 2003) at optical wavelengths, HEBS substrates remain a virtually newborn technology for near-IR applications. To begin to address this gap, we test how HEBS glass optical depths and polychromaticity are affected by using different power electron guns and different electron gun exposure times. We conduct parallel experiments with an Aluminum-coated and bare-surface binary substrate and compare the results.

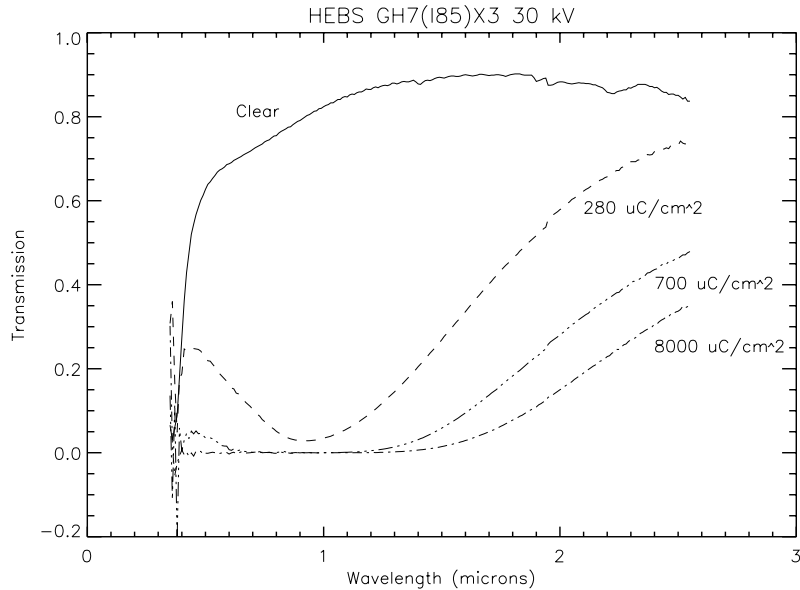


Figure 6. Spectro-photometric transmission curves for 30keV electron gun exposures of HEBS GH7(I85)X3 at 280, 700, and 8000 $\mu\text{C cm}^{-2}$ exposure doses.

3.1. Laboratory Procedures

Our HEBS glass substrate, HEBS GH7(I85)X3, was provided as a sample by Canyon Materials. The substrate was fabricated for optimal performance at near-IR wavelengths, with a 10- μm ion-doped surface layer allowing for the obtainment of large optical depths (>4) upon electron-beam exposure. Each electron beam exposure, performed with a given beam power and exposure time, wrote out a 5mm \times 5mm opaque patch on the substrate. We chose this large shape (as opposed to taking advantage of the electron beam's 0.1- μm resolution) in order to accommodate our particular spectro-photometric measurement setup (described a few sentences from now). We effectively had access to two electron gun power levels: one was a 30keV electron gun operated at Canyon Materials; the other was a 100 keV electron gun operated at JPL. (Electron guns can, in principle, be tuned to many different power settings, but the overhead required in conducting this tuning effectively limits us, for now, to just these two settings.) The 30 keV opaque patches were written at Canyon Materials to dose levels of 280, 700, and 8000 $\mu\text{C cm}^{-2}$. The 100 keV opaque patches, written on the same substrate, were written at JPL to identical dose levels. We made sure to leave a sufficient non-exposed region so that we could measure “clear” throughput as well. To illuminate the substrate for transmission measurements, we used a 100W quartz tungsten halogen lamp in an Oriel Model 7340 Illuminator. Downstream of the exposed substrate, we used an Oriel IS Series 74000 Minispectrometer to step (at 10 nm increments) through the sampled wavelengths and record each resulting intensity (at 15nm bandwidth). For each wavelength step, we recorded the intensity through each opaque patch, through the clear substrate, and through the ambient air (substrate removed). We followed each of these sets with two calibration dark frames (light source off). We calculated “clear” transmission by dividing “clear minus dark” by “air minus dark”. We calculated the opaque patch transmission by dividing “opaque minus dark” by “clear minus dark”. Figures 6, 7, and 8 show the experimental results. The plots reveal that the 100 keV, 8000 $\mu\text{C cm}^{-2}$ setting exhibits the most desirable characteristics, with a stable transmission function and high optical densities (≥ 4.4) through J and H bands (see Figure 8). The true optical depth (OD) and stability could conceivably be significantly larger than the 4.4 OD noise floor, as this boundary is limited by our experimental setup. K-band exhibits a considerably more modest mean optical depth of 2.3 with OD varying by ~ 2 between the short and long wavelength ends.

As a comparison, we conducted parallel spectro-photometric measurements on the binary mask substrate, a 0.125-inch thick fused silica piece (CVI PW-1012UV) with a 100nm-thick Aluminum top-layer. A 5mm \times

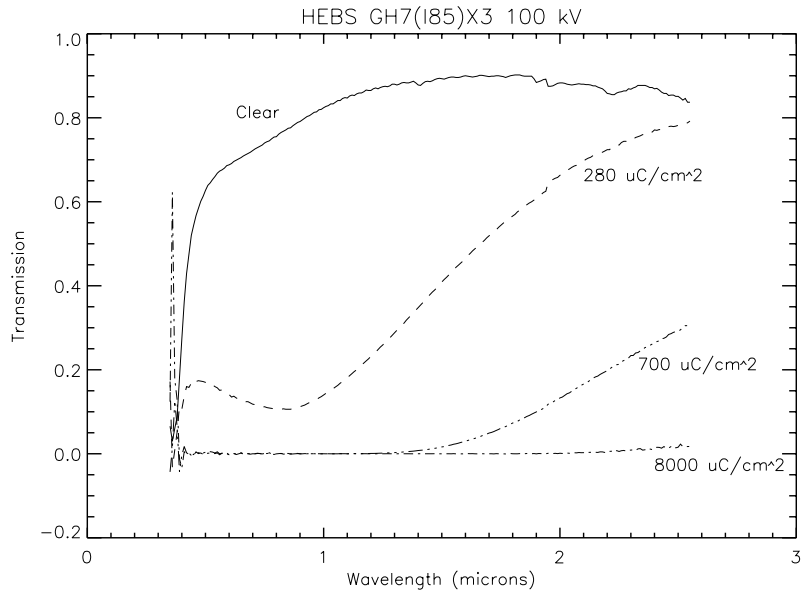


Figure 7. Spectro-photometric transmission curves for 100keV electron gun exposures of HEBS GH7(I85)X3 at 280, 700, and 8000 $\mu\text{C cm}^{-2}$ exposure doses.

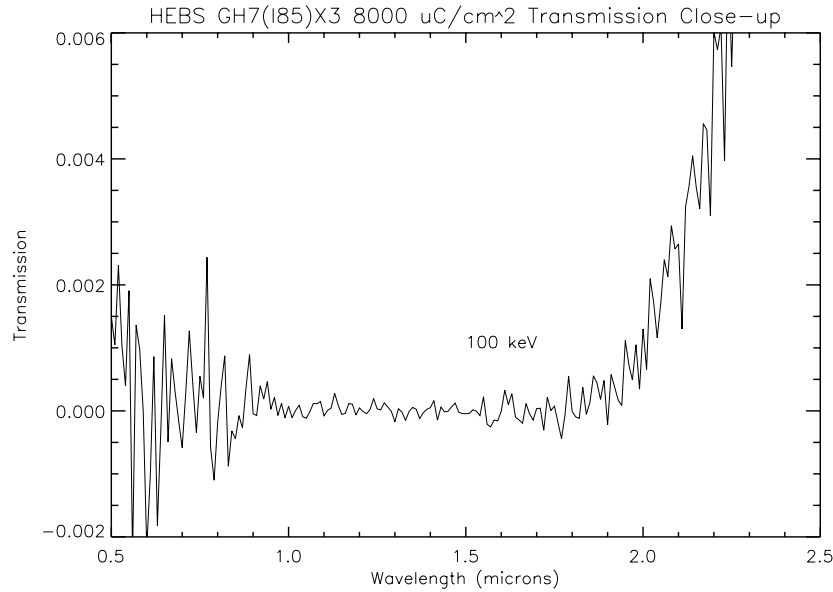


Figure 8. A close-up of the spectro-photometric transmission curve for the 100keV electron gun exposure of HEBS GH7(I85)X3 at 8000 $\mu\text{C cm}^{-2}$. The high-frequency variation represents noise in our experimental measurement rather than true transmission variations. In J (1.13-1.38 μm), H (1.49-1.81 μm), and K (2.0-2.4 μm) bands, our experiment returned mean transmission levels of $1.8 \times 10^{-5} \pm 2 \times 10^{-5}$, $-2.2 \times 10^{-5} \pm 3 \times 10^{-5}$, and $57 \times 10^{-4} \pm 8 \times 10^{-4}$, respectively.

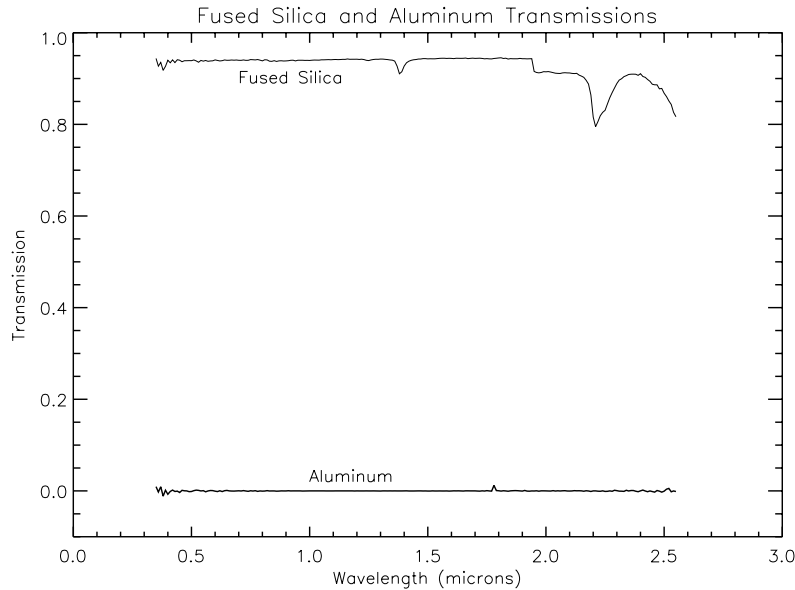


Figure 9. Spectro-photometric transmission curves for bare fused silica and fused silica with a 100nm-thick Al overcoat. The Aluminum-coated substrate exhibits a transmission level of $-1.2 \times 10^{-5} \pm 1.1 \times 10^{-4}$ across the entire 0.5-2.5 μm wavelength regime, as reported by our experiments. The bare fused silica exhibits a typical transmission level $\sim 93\%$ through J (1.13-1.38 μm) and H (1.49-1.81 μm) bands, but fluctuates significantly (around 10%) at K-band (2.0-2.4 μm) wavelengths.

5mm patch of the Aluminum layer was removed using standard lift-off lithography. The opaque and clear region transmission levels were then measured using the techniques described above. Results are displayed in Figure 9. As expected, the Aluminum layer exhibits a very stable, deep opacity ($\text{OD} > 4$) across the entire wavelength regime. Experiment noise prevents us from analyzing optical depths below $\text{OD} = 4$. From Figure 9, one sees that the clear fused silica transmission maintains a typical throughput $\sim 92\%$ in J and H bands, but fluctuates significantly (on the order of 10%) as one moves into K-band wavelengths.

3.2. Mask Transmissions - Discussion

Results portrayed in figures 6 through 9 indicate that, overall, the Al-coated fused silica provides the most stable, deep optical depths over all sampled wavelengths. Comparing HEBS glass 100keV 8000 $\mu\text{C cm}^{-2}$ J and H band exposures with Aluminum transmittance, one sees that both HEBS and fused silica exhibit identical optical depths (given our noise floor of $\text{OD} \sim 4$). Therefore, for these wavelengths, a user must weigh the trade-offs between the binary masks' better "clear" throughput and the HEBS glass' superior resolution for writing specific patterns at precise optical depths. At K-band, the binary mask delivers significantly better optical depths (an improvement of $\text{OD} \sim 2$) compared to the 100keV 8000 $\mu\text{C cm}^{-2}$ HEBS sample. However, the HEBS glass exhibits a more stable "clear" throughput at these wavelengths. If a user specifically desired the HEBS' better K-band "clear" transmission stability or the HEBS glass' precise writing capabilities, a few options exist for potentially improving its poor optical depth. One could subject the HEBS substrate to longer electron-gun exposure times, thus exceeding our 8000 $\mu\text{C cm}^{-2}$ level. Figure 7 suggests that longer exposures deepen opacity. However, we expect the 10- μm ion doped layer to saturate at some level (perhaps it has already happened at 8000 $\mu\text{C cm}^{-2}$), thus limiting the achievable optical depth. An alternative could be to fabricate a HEBS glass substrate with a thicker ion-doped layer than the 10- μm thickness we use for these experiments. However, such increased thickness, while deepening the optical density in electron-exposed patches, could result in a significantly poorer "clear" transmission level (C. Wu, Canyon Materials, private communication, Jan 2005). A third alternative could be to "cement" two fused-silica substrates together, each one with a 10- μm thick ion-doped surface. Further experimental testing would be required to address these speculations.

4. CONCLUSIONS

We have demonstrated here, through a simulated Palomar Adaptive Optics and coronagraphic system, that the implementation of a graded exponential mask in the Palomar AO PHARO camera should improve the detectable magnitude floor by ~ 2.3 -mag in K-band, at separations between 0.75 and 1.5 arcsec. We have also demonstrated that both binary notch-filter (consisting of fused silica with an Al overcoat) and HEBS glass (GH7[I85]X3) both provide adequate technologies to achieve such improvements. In J (1.13-1.38 μm) and H (1.49-1.81 μm) bands, both substrates perform comparably: fused silica possesses a slightly higher and more stable clear transmission, with a transmittance level $\sim 94\%$ and fluctuations within a couple percent; HEBS glass exhibits a transmittance $\sim 85\%$ in these bands with a fluctuation (with wavelength) on order of 5%. In K-band (2.0-2.4 μm), both substrate performances degrade, though both should be able to provide useful graded functions. Simulations indicate that their achievable optical depths are adequate. HEBS has the drawback that its opaque transmission varies from ~ 0.001 to ~ 0.01 between long and short wavelength ends. Al-coated fused silica has a stable opaque region, but its clear transmission varies between about 0.8 and 0.9 across the K-band range. While both substrates should still provide useful tools for high-contrast K-band astronomical imaging, their particular effectiveness would depend on the specific astronomical source and science requirements.

A final motivation for conducting the examination into HEBS and binary notch-filter masks was to further a speculation into whether such masks could be effective for spaced-based missions such as NASA's planned TPF-C or the proposed Eclipse mission. While the baseline design for TPF-C, for instance, entails shorter wavelengths than those examined in this study, the existence of potentially revealing near-IR absorption lines in planet atmospheres (i.e. water, methane) warrants a consideration into expanding this baseline wavelength. The data presented here shows no reason why either HEBS or Al-coated fused silica could not provide adequate graded masks for space-based operations in J and H bands. However, given TPF-C's stringent 10^{-10} required contrast at $4\lambda/D$, significant further investigation would be required: optical densities greater than $\text{OD}=4$ would need to be tested; and in the case of binary masks, the effects of mask-induced polarization would need to be addressed before asserting any robust conclusions.

4.1. Acknowledgments

We thank Chuck Wu (Canyon Materials) for providing us with the HEBS glass sample as well as important guidance in HEBS glass technology. We thank Chris Koresko (JPL) for providing us with copies of his Palomar AO simulation code. We thank John Krist for many fruitful discussions on coronagraph simulation modeling. This work was supported at Caltech/JPL through NASA contract NAS7-03001.

REFERENCES

1. J. C. Carson, S. S. Eikenberry, B. R. Brandl, J. C. Wilson, & T. L. Hayward "The Cornell High-Order Adaptive Optics Survey for Brown Dwarfs in Stellar Systems - I: Observations, Data Reduction, and Detection Analyses," *AJ*, in press.
2. J. H. Debes & J. Ge "High-Contrast Imaging with Gaussian Aperture Pupil Masks" *PASP*, 116, 674, 2004.
3. T. L. Hayward, B. Brandl, B. Pirger, C. Blacken, G. E. Gull, J. Schoenwald, & J. R. Houck "PHARO: A Near-Infrared Camera for the Palomar Adaptive Optics System," *PASP*, 113, 105, 2001.
4. M. J. Kuchner & W. A. Traub, "A Coronagraph with a Band-Limited Mask for Finding Terrestrial Planets," *ApJ*, 570, 900, 2002.
5. M. J. Kuchner, J. Crepp, & J. Ge, "Eighth-Order Masks for Terrestrial Planet Finding," *astro-ph/0411077*, 2004.
6. S. A. Metchev & L. A. Hillenbrand "Initial Results from the Palomar Adaptive Optics Survey of Young Solar-Type Stars: A Brown Dwarf and Three Stellar Companions" *ApJ*, 617, 1330, 2004.
7. B. R. Oppenheimer et al., "The Lyot Project: Toward Exoplanet Imaging and Spectroscopy," *Proc. SPIE*, 5490, 4330, 2004.
8. M. Shao, "Science Overview and Status of the SIM Project," *Proc. SPIE*, 5491, 328, 2004.
9. A. Sivaramakrishnan, C. D. Koresko, R. B. Makidon, T. Berkefeld, & M. J. Kuchner, "Ground-Based Coronagraphy with High-Order Adaptive Optics," *ApJ*, 552, 397, 2001.

10. "Technology Plan for the Terrestrial Planet Finder," C. A Lindensmith ed., JPL Publication 2003-007.
11. J. T. Trauger et al. "Coronagraph Contrast Demonstrations with the High-Contrast Imaging Testbed," *Proc. SPIE*, 5487, 1330, 2004.
12. M. Troy et al. "Palomar Adaptive Optics Project: Status and Performance," *Proc. SPIE*, 4007, 31, 2000
13. D. W. Wilson, P. D. Maker, J. T. Trauger, & T. B. Hull, "Eclipse Apodization: Realization of Occulting Spots and Lyot Masks," *Proc. SPIE*, 4860, 361, 2003.